Active Site Structure of Rieske-Type Proteins: Electron Nuclear Double Resonance Studies of Isotopically Labeled Phthalate Dioxygenase from *Pseudomonas cepacia* and Rieske Protein from *Rhodobacter capsulatus* and Molecular Modeling Studies of a Rieske Center[†,‡]

Ryszard J. Gurbiel,[§,||] Peter E. Doan,[§] George T. Gassner,[⊥] Thomas J. Macke,[▽] David A. Case,[▽] Tomoko Ohnishi,[#] James A. Fee,*[,@] David P. Ballou,[⊥] and Brian M. Hoffman[§]

Department of Chemistry, Northwestern University, Evanston, Illinois 60208, Department of Biological Chemistry, The University of Michigan, Ann Arbor, Michigan 48109-0606, Scripps Research Institute, MB-1, 10666 Torrey Pines Road, La Jolla, California 92037, Johnson Research Foundation and Department of Biochemistry and Biophysics, University of Pennsylvania, Philadelphia, Pennsylvania 19104, and Department of Biology, University of California at San Diego, La Jolla, California 92093

Received February 16, 1996; Revised Manuscript Received April 15, 1996[⊗]

ABSTRACT: Continuous wave electron nuclear double resonance (CW ENDOR) spectra of [δ-^{15}N,ϵ-^{14}N]-histidine-labeled phthalate dioxygenase (PDO) from *Pseudomonas cepacia* were recorded and found to be virtually identical to those previously recorded from [δ,ϵ-$^{15}N_2$]histidine-labeled protein [Gurbiel, R. J., Batie, C. J., Sivaraja, M., True, A. E., Fee, J. A., Hoffman, B. M., & Ballou, D. P. (1989) *Biochemistry 28*, 4861−4871]. Thus, the two histidine residues, previously shown to ligate one of the irons in the cluster [*cf.* Gurbiel *et al.* 1989)], both coordinate the metal at the N(δ) position of their imidazole rings. Pulsed ENDOR studies showed that the "remote", noncoordinating nitrogen of the histidine imidazole ring could be observed from the Rieske protein in a sample of *Rhodobacter capsulatus* cytochrome bc_1 complex uniformly labeled with ^{15}N but not in a sample of PDO labeled with [δ-^{15}N,ϵ-^{14}N]histidine, but this atom was easily observed with a sample of *Rh. capsulatus* cytochrome bc_1 complex that had been uniformly labeled with ^{15}N; this confirmed the conclusion from the CW ENDOR studies that ligation is exclusively via N(δ) for both ligands in the PDO center. Modifications in the algorithms previously used to simulate ^{14}N ENDOR spectra permitted us to compute spectra without any constraints on the relative orientation of hyperfine and quadrupole tensors. This new algorithm was used to analyze current and previously published spectra, and slightly different values for the N−Fe−N angle and imidazole ring rotation angles are presented [*cf.* Gurbiel *et al.* (1989) Gurbiel, R. J., Ohnishi, T., Robertson, D. E., Daldal, F., and Hoffman, B. M. (1991) *Biochemistry 30*, 11579−11584]. This analysis has permitted us to refine the proposed structure of the [2Fe-2S] Rieske-type cluster and rationalize some of the properties of these novel centers. Although the spectra of cytochrome bc_1 complex from *Rh. capsulatus* are of somewhat lower resolution than those obtained with samples of PDO, our analysis nevertheless permits the conclusion that the geometry of the cluster is essentially the same for all Rieske and Rieske-type proteins. Structural constraints inferred from the spectroscopic results permitted us to apply the principles of distance geometry to arrive at possible three-dimensional models of the active site structure of Rieske protein from *Rh. capsulatus*. Results from this test case indicate that similar procedures should be generally useful in metalloprotein systems. We also recorded the pulsed and CW ENDOR spectra of ^{57}Fe-labeled PDO, and the resulting data were used to derive the full hyperfine tensors for both Fe(III) and Fe(II) ions, including their orientations relative to the **g** tensor. The **A** tensor of the ferric ion is nominally isotropic, while the **A** tensor of the ferrous ion is axial, having $A_{||} > A_{\perp}$; both tensors are coincident with the observed **g** tensor, with $A_{||}$ of the ferrous ion lying along the maximum *g*-value, g_1. These results were examined using refinements of existing theories of spin-coupling in $[2Fe\text{-}2S]^{+}$ clusters, and it is concluded that current theories are not adequate to fully describe the experimental results.

Rieske-type iron−sulfur proteins were first recognized as components of mitochondrial respiration [*cf.* Rieske (1976), Trumpower (1990), and Trumpower and Gennis (1994) for review] and later as cofactors in various dioxygenases of bacterial origin [*cf.* Blumberg and Peisach (1974), Fee *et al.* (1986), Batie and Ballou (1990), and Mason and Cammack (1992) for review]. The Rieske iron-sulfur protein contains

[⊗] Abstract published in *Advance ACS Abstracts,* June 1, 1996.

[†] Supported by grants from the United States Public Health Service (HL 1353 to B.M.H., GM20877 to D.P.B., GM35342 to J.A.F., HL 51030 to DAC) and the National Science Foundation (DMB-89-07559 to B.M.H. and MCB-94-18694 to T.O.).

[‡] We dedicate this article to Professor Bernard L. Trumpower.

* Address requests for reprints to this author.

[§] Northwestern University.

[||] Present address: Institute of Molecular Biology, Jagiellonian University, Kraków, Poland.

[⊥] The University of Michigan.

[▽] Scripps Research Institute.

[#] University of Pennsylvania.

[@] University of California at San Diego.

S0006-2960(96)00380-7 CCC: $12.00

Scheme 1

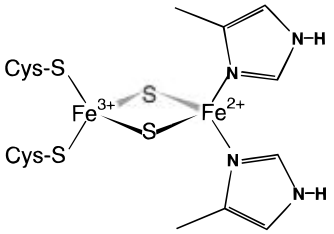

a [2Fe-2S] cluster that exhibits spectral and chemical properties that distinguish it from the analogous [2Fe-2S] cluster of plant ferredoxins where the cluster is coordinated by four cysteine thiolates, two to each iron [*cf.* Blumberg and Peisach (1974), Bertrand and Gayda (1979), Fee *et al*. (1984), Bertrand *et al*. (1985), Britt *et al*. (1991), Liebl *et al*. (1992), and Shergill and Cammack (1994) for review]. Electronic spin coupling between the high-spin ferric ions of the plant ferredoxins has been examined in great detail [*cf.* Sands and Dunham (1975) Bertrand *et al*. (1985)], and the spin coupling in the Rieske cluster must be generally similar. Thus, in the fully oxidized proteins, the spins of the two Fe(III) atoms are coupled to produce an EPR silent ground state, while in the one-electron reduced forms, the Fe(III) and Fe(II) are coupled to yield an EPR detectable, $S = {}^1/_2$ ground state. One spectral feature that distinguishes the reduced Rieske from the plant ferredoxins is its average EPR *g*-value. The latter typically have *g*-values of 2.04, 1.95, and 1.87 with $g_{av} \approx 1.96$, whereas the former typically have *g*-values of 2.02, 1.90, and 1.80 with $g_{av} \approx 1.91$. The lower g_{av} of the Rieske-type proteins was recognized (Blumberg & Peisach, 1974; Bertrand & Gayda, 1979) as indicating significantly different bonding to the spin-coupled [2Fe-2S] cluster in the two classes of proteins. It is now known that this reflects the increased ligand field arising from imidazole coordination to the Fe(II) ion in the Rieske proteins [*cf.* Bertrand *et al*. (1985) and Gurbiel *et al*. (1989) for review]. Previous ENDOR[1] studies of the Rieske-type centers in PDO and the bc_1 complex, in which the proteins had been selectively enriched with [δ,ϵ-$^{15}N_2$]histidine or uniformly enriched with ^{15}N, unambiguously showed that two histidine residues were coordinated to the cluster (Gurbiel *et al*. 1989, 1991), which when combined with earlier Mössbauer results (Fee *et al*. 1984) led to a model of the active site of these proteins consisting of a [2Fe-2S] cluster in which one of the irons is coordinated to two cysteine thiolates while the other iron is coordinated to the imidazole rings of two histidine residues, as shown in Scheme 1.

To further explore the electronic properties of the Rieske center and refine our knowledge of its structure, we report analyses for ENDOR spectra of samples of PDO obtained from *Pseudomonas cepacia* enriched with either ^{57}Fe or [δ-^{15}N]-histidine isolated from a histidine auxotroph grown on [δ-^{15}N,ϵ-^{14}N]histidine (PDO($^{15}N(\delta)$)) and of a Rieske protein, associated with the cytochrome bc_1 complex isolated from *Rhodobacter capsulatus* grown on [^{15}N]$(NH_4)_2SO_4$ (bc_1-(^{15}N(u))). Our analyses of the ENDOR data place several constraints on the three-dimensional atomic structure surrounding the [2Fe-2S] cluster, and these have permitted us to apply the principles of distance geometry [*cf.* Crippen and Havel (1988)] to obtain possible structural models of the Rieske active site. The results of this test case suggest that such a combination of approaches will have considerable applicability in the studying of metalloenzyme active site structure. We further report that existing theories of electronic spin coupling in $[2Fe\text{-}2S]^+$ clusters appear inadequate to fully describe ENDOR-derived ^{57}Fe hyperfine coupling tensors of the two Fe ions.

[1] Abbreviations: ENDOR, electron nuclear double resonance; EFG, electric field gradient; PDO, phthalate dioxygenase; BC1, cytochrome bc_1 or bc_1 indicates intact cytochrome bc_1 complex from *Rhodobacter capsulatus*; PDO($^{15}N(\delta)$), PDO labeled with [δ-^{15}N,ϵ-^{14}N]histidine; PDO(^{15}N(u)), PDO uniformly labeled with ^{15}N; bc_1(^{15}N(u)), uniformly ^{15}N-labeled cytochrome bc_1 complex.

MATERIALS AND METHODS

Sample Preparation. D,L-[δ-^{15}N]Histidine was synthesized by the reaction of K[^{15}N]CN with L-2,5-diamino-4-ketovaleric acid as described by Hunkapiller *et al.* (1973, and references therein) and was a generous gift from Dr. William Bachovchin. When that substance was dissolved into D_2O/DNO_3, the one-dimensional NMR spectrum of this material showed a single, sharp ^{15}N resonance near 200 ppm [*cf.* Bachovchin *et al*. (1986)]. Samples of uniformly ^{15}N-labeled cytochrome bc_1 complex from *Rh. capsulatus* were obtained as described previously (Gurbiel *et al*., 1991). Phthalate dioxygenase was purified by the method of Batie *et al*. (1987). A histidine auxotroph of *Ps. cepacia* (DB0110) was a gift from Dr. Ron Olsen and was grown as described by Bull and Ballou (1981) except that the culture medium contained ~1 mM D,L-[δ-^{15}N]histidine. ^{57}Fe was obtained from Amersham, and PDO was isolated from wild type cells grown on 21 μM $^{57}FeSO_4$. Enzyme samples were 0.8 mM and were adjusted to contain ~50% ethylene glycol. They were placed in quartz capillary tubes, reduced with a slight excess of sodium dithionite, and stored in liquid nitrogen.

ENDOR Measurements and Theory. Continuous wave (CW) ENDOR spectra were recorded on a Varian Associates E-110 spectrometer (35 GHz, Q-band) as described elsewhere (Werst *et al*., 1991). Pulsed ENDOR [*cf.* Gemperle and Schweiger (1991)] spectra at X-band were recorded on a spectrometer described by Fan *et al.* (1992). Q-Band pulsed ENDOR spectra were recorded on a spectrometer described by Davoust *et al.* (1996).

For a single orientation of a paramagnetic center [*cf.* Abragam and Bleaney (1970)], the ENDOR spectrum of a nucleus (J) of spin *I* consists, in principle, of 2*I* transitions at frequencies given to the first approximation by eq 1

$$\nu_{\pm}(m_I) = \left|\pm\frac{A(\mathrm{J})}{2} + \nu(\mathrm{J}) + \frac{3P(\mathrm{J})}{2}(2m_I - 1)\right| \quad \text{where} \quad -I + 1 \le m_I \le I \quad (1)$$

Here A(J) and P(J) are the angle-dependent hyperfine and quadrupole coupling constants, respectively, which are molecular parameters and independent of the spectrometer microwave frequency, and ν(J) is the nuclear Larmor frequency, ($\nu(\mathrm{J}) = g_n\beta_n H$). The ^{15}N nucleus has $I = {}^1/_2$, and its ENDOR pattern consists of a doublet centered at $A(^{15}N)/2$ having lines separated by $2\nu(^{15}N)$. The hyperfine couplings and Larmor frequencies of two nitrogen isotopes obey the relation

$$\left|\frac{\nu(^{15}\mathrm{N})}{\nu(^{14}\mathrm{N})}\right| = \left|\frac{A(^{15}\mathrm{N})}{A(^{14}\mathrm{N})}\right| = 1.403 \qquad (2)$$

Thus, the assignment of an ENDOR spectrum for one isotope directly predicts features of the other one. The samples employed in this study are frozen solutions and thus contain a random distribution of all protein orientations. As reviewed in detail (Gurbiel *et al.*, 1989; Hoffman *et al.*, 1993) the principal values of a hyperfine tensor and its orientation relative to the **g** tensor axis frame can be determined by simulating a set of ENDOR spectra recorded at *g*-values (fields) across the EPR envelope.

Molecular Modeling. Peptide conformations were constructed using metric matrix distance geometry (Crippen and Havel, 1988). Upper and lower distance bounds were determined from the covalent geometry for atoms separated by three bonds or less; lower bounds were set to the sum of atomic radii (see caption to Figure 7) for atoms separated by more than three bonds. The triangle smoothing of the distance bounds, conversion into three-dimensional structures, and subsequent refinement against distance bounds was carried out using the NAB program (Macke, 1996) and followed closely the protocols used in the DGEOM program (Blaney *et al.*, 1990; Peishoff and Dixon, 1992). After distance geometry refinement, the peptide coordinates were subjected to 15 000 steps of energy minimization followed by molecular dynamics simulated-annealing refinement (Gippert *et al.*, 1990) using the AMBER all-atom force field (Weiner *et al.*, 1986); the geometry of the core segment was kept fixed except for allowing free rotation about the γ angles. The simulated-annealing refinements consisted of 15 ps of molecular dynamics simulation, with the structures heated to 600 K over the first 6 ps and then cooled back to 0 K over the subsequent 9 ps, in a manner similar to NMR refinement simulations [for further details, see Moore *et al.* (1991)]. We chose representative β and γ angles in the allowed region (see Table 3 and Figure 7) as starting points in attempts to build models of the core complexed to the peptide fragments CysThrHisLeuGlyCys (1) and CysProCysHis (2), where the core is coordinated to the first and third residues of peptide 1 and to the first and fourth residues of peptide 2, with a disulfide bond between residue 6 of peptide 1 and residue 3 of peptide 2. A total of 100 structures were determined for each of the starting core geometries given in Table 3; from each group, the 50 structures with the lowest AMBER energies after simulated annealing were retained for statistical analysis. Overall, this procedure should sample widely the peptide structures that are allowed given the constraints we have assumed, but the calculations take no account of the influence of the remainder of the polypeptide chain or the solvent environment. Additional details are found in the legends to Figures 7 and 8.

RESULTS

CW and Pulsed ENDOR of Nitrogen. The EPR spectrum of PDO is unchanged by substitution of isotopes, with *g*-values of $g_1 = 2.01$, $g_2 = 1.91$, and $g_3 = 1.7$. ^{15}N ENDOR spectra were collected from PDO(^{15}N(δ)) at numerous fields across the EPR envelope, and these are shown in Figure 1A−F along with corresponding spectra from PDO(^{15}N(u)) (middle) and simulations (bottom, see below). Figure 1A is a "single-crystal" spectrum taken at the low-field, $g_1 =$ 2.01, edge of the EPR envelope; panels B and C of Figure 1 show spectra recorded at *g*-values between g_1 and g_2, and panels D−F of Figure 1 show spectra recorded at *g*-values between g_2 and g_3. The earlier analysis of the spectra for PDO(^{15}N(u)) showed that each of the two peaks in Figure 1A corresponds to the ν_+ resonance of a ^{15}N-labeled histidine bound to the Fe^{2+} ion of the cluster (Gurbiel *et al.*, 1989). The peak at $\nu_+ \approx 9.6$ MHz is associated with the histidine ligand denoted N(2), and according to eq 1, $A(^{15}\mathrm{N}(2)) \approx$ 8.4 MHz; the peak at $\nu_+ \approx 8.6$ MHz is from ligand N(1) and corresponds to $A(^{15}\mathrm{N}(1)) \approx 6.4$ MHz. (Note that these values do not correspond to principal values of a hyperfine tensor.) Although the patterns spread out in the spectra taken at higher fields, the two peaks persist and the analysis showed that, here too, the intensity of each is primarily associated with a single ^{15}N; the shoulders to higher frequencies typically have significant contributions from both N(1) and N(2) [*cf.* Gurbiel *et al.* (1989)].

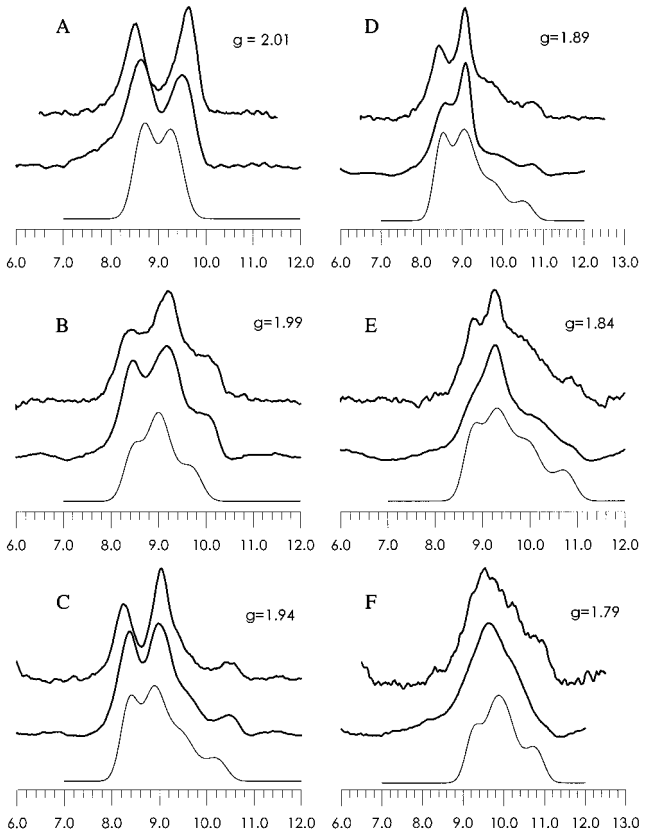

FIGURE 1: CW ENDOR (35 GHz) spectra of *Ps. cepacia* phthalate dioxygenase (PDO) taken at different *g*-values across the EPR envelope. In each case, the upper spectrum is from PDO(^{15}N(δ)), the middle one is from PDO(^{15}N(d)), and the bottom one is the simulated spectrum. The conditions of the experiments were as follows: temperature, 2 K; microwave frequency, 35.2 GHz; microwave power, 0.16 mW; 100 kHz field-modulation amplitude, 2.5 G; RF power, 30 W; scan rate, 2.5 MHz/s; and 400 scans. The parameters of the simulations were as follows: ENDOR line width, 0.25 MHz; and EPR line width, 40 G.

Comparison of the corresponding spectra from PDO(^{15}N(u)) and PDO(^{15}N(δ)) shows that all the features are reproduced in each spectrum; at each field, the frequencies of these features match to within the experimental uncertainty of about ±0.2 MHz, and to a first approximation, the intensities of the various features also match. These observations indicate that both N(1) and N(2) are the δ-nitrogens of histidyl imidazole bound to the cluster.

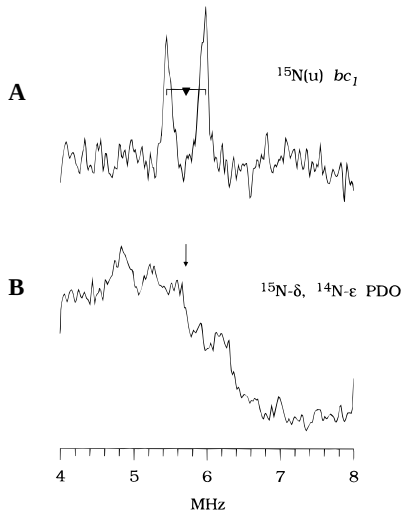

FIGURE 2: Pulsed Mims ENDOR spectra (35 GHz) of [δ,ϵ-$^{15}N_2$] histidine (^{15}N(u))-labeled cytochrome bc_1 complex from *Rh. capsulatus* (A) and [δ-^{15}N] histidine-labeled phthalate dioxygenase from *Ps. cepacia* (B) showing that the remote ^{15}N ENDOR in ^{15}N(u) bc_1 is associated with the ϵ site and not the δ site of the histidine. The EPR signal in panel B is 40 times that of panel A. The Larmor frequencies of ^{15}N for the two spectra are shown by the ▼ in panel A and the arrow in panel B. The observed coupling in panel A is 0.51 MHz. The conditions were as follows: temperature, 2 K; microwave frequency, 35.36 GHz; microwave pulse width, 50 ns; τ_{12}, 720 ns; RF pulse width, 60 μs; RF power, 300 W; 256 points per spectrum; and number of transients per point, (A) 720 and (B) 144.

We have used Mims (stimulated echo) pulsed ENDOR at Q-band [*cf.* Gemperle and Schweiger (1991)] to examine the "remote", noncoordinated nitrogens of the bound histidines. In earlier papers [*cf.* Hoffman *et al*. (1993)], we showed that Mims ENDOR [*cf.* Gemperle and Schweiger (1991)] is a particularly effective method for studying weakly coupled ($A < 2$ MHz) nuclei. The spectra in Figure 2 correspond to the ENDOR from the noncoordinated (remote) nitrogen of the bc_1(^{15}N(u)) complex (upper) and from PDO labeled with [δ-^{15}N,ϵ-^{14}N]histidine (lower). In the BC1 sample, at $g = 1.91$, using a Mims ENDOR sequence with $\tau = 680$ ns, the spectrum consists of only two very sharp lines centered at 5.66 MHz [ν(^{15}N) at 13.1 kG], with a hyperfine coupling constant of ≈0.51 MHz. The two lines are considered to arise from the two histidine imidazole rings, both of which are labeled with ^{15}N. Because this is not a single-crystal-like position, the absence of orientation-selective broadening of the lines indicates that the hyperfine tensor for this site is nominally isotropic. A spectrum taken under identical conditions using PDO(^{15}N(δ)) shows only broad unresolved ENDOR lines in this frequency region, despite the fact that the EPR signal of this sample is 40 times stronger than that of the bc_1 (^{15}N(u)) complex.[2] Thus, we confirm that the ^{15}N-(δ) PDO sample has ^{14}N(ϵ), rather than ^{15}N nuclei, at the remote sites that give rise to the 0.5 MHz coupled ENDOR transitions in bc_1 (^{15}N(u)). We note further that the very weak hyperfine coupling to the ^{15}N(ϵ) corresponds to an even smaller ^{14}N(ϵ) coupling, and this precludes observation of any significant ESEEM from ^{14}N(ϵ). The CW and pulsed ENDOR spectra shown in Figures 1 and 2 permit the conclusion that in PDO the imidazole rings of both coordinating histidine residues bind to the Fe at their N(δ) position.[3] Our observations do not bear directly on which N atoms of the imidazole ring bind to Fe in BC1. However, the near identity of all spectral features of the two proteins suggests very strongly that the three-dimensional structure in the immediate environment of the [Fe-S] clusters is nearly identical in both proteins.

Table 1: Hyperfine Tensor Principal Values (Megahertz) and Orientation (Degrees) Relative to **g** Tensor Principal Axes for the ^{15}N Ligands in PDO and BC1

	PDO		BC1 new simulations	
	site 1	site 2	site 1	site 2
		Principal Values		
A_1	5.4 (0.2)	6.3 (0.2)	5.2 (0.2)	6.0 (0.2)
A_2	5.5 (0.1)	6.7 (0.1)	5.8 (0.1)	6.5 (0.1)
A_3	8.4 (0.2)	10.2 (0.2)	8.5 (0.3)	9.6 (0.3)
		Euler Angles		
α^a	0 (10)	0 (10)	0 (10)	0 (10)
β^b	38 (3)	45 (3)	35 (5)	45 (5)
γ^b	—[c]	—[c]	—[c]	—[c]

[a] α is defined as the angle of rotation of either of the Fe−N axes around the g_3 axis. [b] β and γ are defined in Scheme 3. [c] γ cannot be determined solely from analysis of the ^{15}N data because the ^{15}N hyperfine tensor is so close to axial, with the unique axis along Fe−N.

Scheme 2

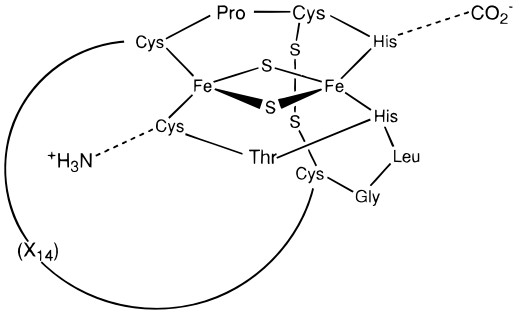

A revised version of the simulation program was recently described (Gurbiel *et al*., 1993). The ^{15}N ENDOR spectra of PDO collected at several points within the EPR envelope, as well as those previously reported for the Rieske center of the bc_1 complex (Gurbiel *et al*., 1991), were analyzed using the new algorithm. The hyperfine tensors for PDO that result from these simulations are presented in Table 1 (see also Scheme 2, above). The principal values for ^{15}N(1) differ only slightly from those previously reported; A_1 is increased by ∼1 MHz, while the other principal values, including the rotation angles, are nearly unchanged. Those for ^{15}N(2) are also nearly unchanged; in particular, the principal values of the hyperfine tensor are, within error, the same. The

[2] The ability to see the ^{15}N ENDOR of such a weakly coupled nucleus does not necessarily imply the ability to see the ^{14}N ENDOR of the same site. The ^{15}N resonances are relatively easily observed because the hyperfine interaction is effectively isotropic and the line widths are extremely narrow. The quadrupole splitting of the ^{14}N nucleus would dominate the appearance of the ^{14}N spectrum, spreading the resonances over an ∼3 MHz range.

[3] Comparison of the ^{15}N ENDOR spectra of the two protein samples indicates a somewhat lower resolution for PDO(^{15}N(δ)), especially in the g_2-g_3 region (data not shown). Although this may reflect sample variability, we note that, with PDO(^{15}N(δ)), all other nitrogens are the ^{14}N ($I = 1$) isotope, while in the PDO(^{15}N(u)), they are ^{15}N ($I = 1/2$). An analogous isotope-dependent resolution was observed in our earlier studies; the [^{14}N] spectra of PDO grown with ^{14}N histidine in a ^{15}N background are better-resolved than those of natural abundance (all ^{14}N) enzymes (Gurbiel *et al*., 1989).

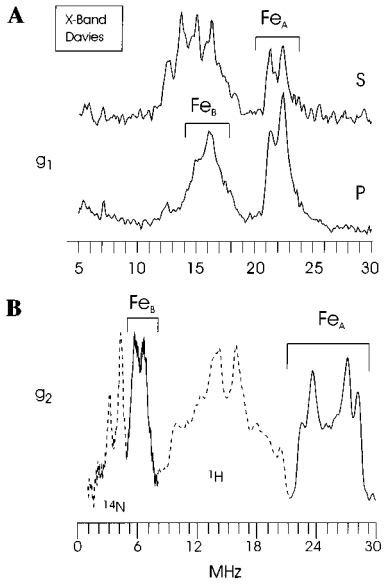

FIGURE 3: Pulsed Davies ENDOR spectra (9.5 GHz) of ^{57}Fe-labeled phthalate dioxygenase from *Ps. cepacia*. (A) Davies ENDOR at g_1 taken with two different microwave pulse widths. Spectrum S is taken under conditions that are close to optimum for proton ENDOR in this protein. Only Fe_A and a series of proton peaks centered at 14.8 MHz are observed clearly. Spectrum P is taken under conditions that suppress the weakly coupled protons, revealing the broad underlying ENDOR from Fe_B. (B) Davies ENDOR spectra taken at g_2 clearly showing peaks from both Fe_A and Fe_B (solid lines). Frequency regions with peaks from ^{1}H and ^{14}N are shown in dashed lines. The experimental conditions were as follows and were: common to all spectra: temperature, 4.2 K; microwave frequency, 9.49 GHz; RF pulse width, 20 μs; repetition rate, 33 Hz; and 256 points per spectrum. (A, Spectrum S) Magnetic field, 0.3360 T; microwave pulse widths, 120−60−120 ns; τ_{23}, 312 ns; and 180 transients. (A, Spectrum P) Magnetic field, 0.3360 T; microwave pulse widths, 40−20−40 ns; τ_{23}, 268 ns; and 144 transients. (B) magnetic field, 0.3526 T; 1−9 MHz region, microwave pulse widths, 64−32−64 ns; τ_{23}, 288 ns; and 160 transients; 5−25 MHz region: microwave pulse widths, 40−20−40 ns; τ_{23}, 288 ns; and 96 transients.

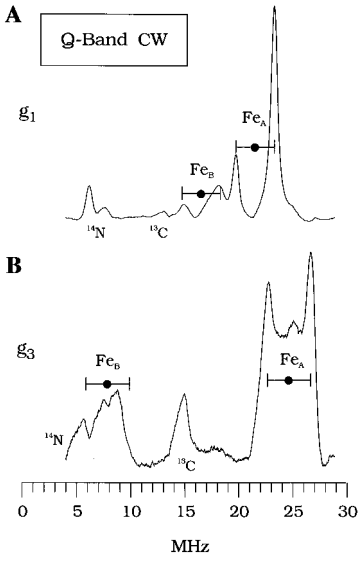

FIGURE 4: CW ENDOR spectra (35 GHz) of ^{57}Fe-labeled *Ps. cepacia* phthalate dioxygenase at the two edges of the EPR envelope. The ^{57}Fe resonances are centered at $A/2$ (●) and split by $2\nu(^{57}\text{Fe})$ (|—|). (A) Spectrum taken at the g_1 (low-field edge) of the EPR envelope. Both the Fe_A and Fe_B resonances lie at higher frequencies than the ^{14}N and ^{13}C resonances. (B) ENDOR spectrum taken at g_3 (high-field edge) of the EPR envelope. Fe_B has shifted to lower frequencies and partially overlaps the ^{14}N resonances in the 4−10 MHz region. The experimental conditions were as follows: temperature, 2 K; microwave frequency, 35.2 GHz; microwave power, 0.16 mW; 100 kHz field-modulation amplitude, 2.5 G; RF power, 30 W; RF band width, 100 kHz; scan rate, 2.5 MHz/s; and 100 scans.

principal tensor values for BC1 are all increased by ∼1 MHz, and the rotation angle β has increased significantly.

CW and Pulsed ENDOR of Iron. The X-band Davies pulsed ENDOR [*cf.* Gemperle and Schweiger (1991)] spectrum of ^{57}Fe ($I = {}^1/_2$)-enriched PDO taken at the low-field, g_1 edge of the EPR envelope is shown in Figure 3 (g_1, upper). The spectrum shows intensity in the range ∼12−19 MHz that arises, at least in part, from ^{1}H ENDOR, but it also shows a doublet centered at ∼22 MHz that is split by twice the Larmor frequency of iron [2ν(Fe) ∼ 1 MHz]. This doublet is absent from a sample containing predominantly ^{56}Fe ($I = 0$), and it is assigned to one of the Fe atoms, denoted Fe_A, with $A(Fe_A) \approx 43$ MHz at g_1. This assignment is consistent with the corresponding Q-band CW ENDOR spectrum at g_1 (Figure 4, g_1), which also shows a doublet centered at $A(Fe_A)/2 \sim 22$ MHz and is split by twice the Larmor frequency of iron at 35 GHz [2ν(Fe) ∼ 3.4 MHz]. Note that the greater intensity of the ν_+ line of the ^{57}Fe compared to its ν_- counterpart is common with Q-band CW ENDOR.

Careful examination of the g_1 CW Q-band ENDOR spectrum (Figure 4, g_1) of the ^{57}Fe-enriched protein reveals an additional doublet that apparently arises from the second iron site, Fe_B. The signal is centered at $A(Fe_B)/2 \sim 16.5$ MHz and split by 2ν(Fe) ≈ 3.4 MHz. Again, this signal is not present in samples containing the natural abundance of ^{57}Fe. When a g_1 X-band Davies pulsed ENDOR [*cf.* Gemperle and Schweiger (1991)] spectrum is collected under "POSHE" conditions [*cf.* Doan *et al*. (1991)] that strongly suppress proton lines (Figure 3A, g_1, lower), it also shows a broad ^{57}Fe feature centered at $A(Fe_B)/2 \sim 16$ MHz, thus confirming the above assignment.

A set of $^{57}Fe_A$ spectra collected in the Davies pulsed mode at g-values across the EPR envelope (Figure 5) was used to analyze the $^{57}Fe_A$ coupling tensor. The field-dependent variation of signals shown in Figure 5 is the classical "triangle" pattern [*cf.* Gurbiel *et al*. (1993)] associated with rhombic and coaxial **g** and **A** tensors where the hyperfine couplings are large compared to 2ν(Fe). The principal hyperfine values are at the centers of the doublets at $g_1(A_1/2)$, $g_2(A_2/2)$, and $g_3(A_3/2)$; they are $\mathbf{A}(Fe_A) = [A_1, A_2, A_3] = [43, 56, 50]$ MHz (Table 2).

The detection and analysis of the $^{57}Fe_B$ signals at fields other than g_1 is more difficult because the hyperfine tensor is highly anisotropic. The experiment requires a simultaneous analysis of both CW Q-band and pulsed X-band data, and even then, the results are less precise than in the case of Fe_A. As the magnetic field is increased from g_1, the $^{57}Fe_B$ peaks move rapidly toward lower frequency and broaden, effectively disappearing at intermediate g-values in the Q-band CW spectrum. However, if the X-band pulsed spectrometer is properly set, ^{57}Fe signals can be detected near g_2 (Figure 3, g_2) as a doublet centered at ∼6.5 MHz ($A \approx$ 13 MHz), which is not present in the natural-abundance sample. At the g_3 (high-field) edge of the EPR envelope, the Q-band $^{57}Fe_B$ ENDOR spectrum again shows an $^{57}Fe_B$ doublet, centered at $A(Fe_B) \approx 7.5$ MHz (Figure 4, g_3). These observations are consistent with an axial ^{57}Fe(B) hyperfine

Table 2: Observed Hyperfine Coupling Constants (Megahertz) for Selected [2Fe-2S] Clusters[a]

		ferrous site			ferric site		
		g_1	g_2	g_3	g_1	g_2	g_3
phthalate dioxygenase[b]	**A**	33.0 ± 0.5	13.0 ± 0.5	14.0 ± 1.0	43.0 ± 0.5	55.0 ± 0.5	50.0 ± 0.5
	V[c]			$V_{2z'}{}^c > 0$			
Thermus Rieske protein	**A**	33 ± 1.5	14 ± 1.5	11 ± 3	43 ± 3	55 ± 3	50 ± 3
	V			$V_{2z'}{}^c > 0$			
adrenodoxin, putidaredoxin[d]	**A**	35 ± 1.5	24 ± 4	17 ± 4	43 ± 1.5	56 ± 2	50 ± 1.5
	V			$V_{2z'} > 0$			
plant ferredoxin[e]	**A**	36.5 ± 0.5	15.0 ± 0.7	13.0 ± 0.4	42 ± 0.4	50.0 ± 2	51.6 ± 0.3
	V	$V_{2z'} < 0$					

[a] In all cases **A**, **g**, and quadrupole, **V** tensors are coaxial. The **g** tensors are defined with $g_1 > g_2 > g_3$. In all cases, the ferrous ion quadrupole tensor is axial; $V_{2z'}$ is the unique principal value, and its correspondence with the **A** tensor is given in the table. We are not concerned with the ferric ion quadrupole tensors. [b] This work. [c] Fee *et al.* (1984). Tensors are oriented relative to **g** so as to match those of PDO. [d] Fritz *et al.* (1971). [e] Fritz *et al.* (1971) and Anderson *et al.* (1975). The numbers quoted are for algal ferredoxin; the measured values for spinach and parsley ferredoxins are the same, within experimental error.

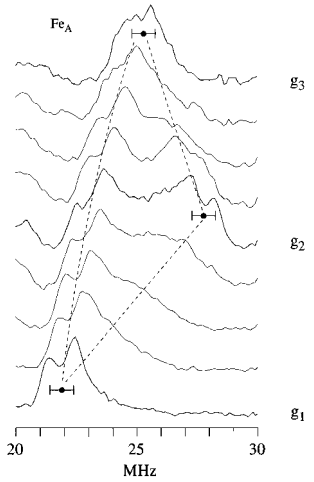

FIGURE 5: Pulsed Davies ENDOR spectra (9.5 GHz) of ^{57}Fe-labeled PDO across the EPR envelope. Only the Fe_A frequency region is shown. The resonances follow a "triangle" pattern (denoted by the dashed lines) for a rhombic **g** and **A** tensor that are coaxial. The three principal hyperfine components ($A/2$) (●) are assigned at g_1, g_2, and g_3. The patterns are centered at $A/2$ and split by $2\nu(^{57}Fe)$ (|—|). The experimental conditions were as follows: temperature, 4.2 K; microwave frequency, 9.45 GHz; microwave pulse widths, 40−20−40 ns; τ_{23}, 270 ns; RF pulse width, 20 μs; RF power, 400 W; 100 points per spectrum; 33 Hz repetition rate; number of transients between, 160 (g_3) and 96 (g_2); and g-values from the top, 1.78, 1.81, 1.85, 1.89, 1.92, 1.94, 1.96, 1.98, and 2.01.

Table 3: Core Geometries Used for Molecular Modeling

group	β	$\gamma_1{}^a$	$\gamma_2{}^a$
1	40	−100	80
2	50	−130	50
3	50	−100	80
4	50	*b*	*b*
5	50	−50	−10

[a] Subscripts on the γ angles refer to peptides 1 and 2, as described in the text. [b] γ angles were not restricted in this starting structure; in all cases, the γ angles were allowed to move freely during the simulated annealing cycle.

tensor that is coaxial with the **g** tensor and has principal values of $\mathbf{A}(Fe_B) = [33, 13, 14]$ MHz [Table 2, Fe(II) site]. The tensor components of Fe_A and Fe_B are indistinguishable from those obtained from Mössbauer studies of the corresponding ferric and ferrous ions of the *Thermus* Rieske cluster (Table 2; Fee *et al.*, 1984).

Molecular Modeling. Neidle *et al.* (1991) and Davidson *et al.* (1992) recently compared and analyzed available amino

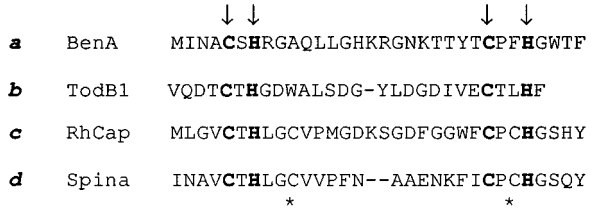

FIGURE 6: Comparison of representative "active site" amino acid sequences of the four known classes of Rieske-type proteins. (*a*) BenA, benzoate dioxygenase from *Acinetobacter calcoaceticus*, accession number P07769. (*b*) TodB1, a small iron−sulfur protein involved in bacterial degradation of toluene (Neidle *et al.*, 1991). (*c*) RhCap, Rieske protein from the bc_1 complex of *Rh. capsulatus*, accession number P08500. (*d*) Spina, Rieske protein from the b_6f complex of spinach. Rieske protein sequences, *c* and *d*, have two additional conserved cysteine residues as indicated by the * below sequence *d*.

acid sequences of Rieske-type proteins. There are four classes of such proteins, and one example of each is shown in Figure 6: bacterial dioxygenases, analogous to PDO, including toluene, naphthalene, benzoate, and benzene dioxygenases (Figure 6, *a*); unfortunately, the sequence of *P. cepacia* PDO was completed only as the manuscript was being submitted for publication.[4] Small Rieske-type proteins carry out electron transfer functions in several of the multicomponent dioxygenases (Figure 6, *b*). Rieske proteins are part of the cytochrome bc_1 complex and involved in respiratory electron transport (Figure 6, *c*). And, Rieske proteins are part of the cytochrome b_6f complex and are involved in photosynthetic electron transport (Figure 6, *d*). These proteins have different molecular weights and different redox properties (Trumpower, 1990; Mason & Cammack, 1992). Nevertheless, all the residues involved in coordination of the [2Fe-2S] cluster reside in a stretch of ≤28 amino acids characterized by the general pattern CysXHis(X)15−21CysXXHis. As pointed out by Davidson *et al.* (1992), in order for the two Cys residues to coordinate one Fe of the [2Fe-2S] cluster and for the two His residues to coordinate to the other Fe, "the intervening region between the

[4] The relevant sequence of *Ps. cepacia* PDO is CPHRRASLVY-GRNEDSGLRCLYH (personal communication from C.-H. Chang and G. J. Zylstra to D. P. Ballou). Additional sequences have appeared in the literature since 1992, and these have been analyzed and consensus sequences assigned for the four different classes of proteins containing the Rieske-type center (D. P. Ballou and G. T. Gassner, unpublished). Preliminary considerations suggest that substitution of proline for threonine in peptide 1 has no effect on the outcome of the theoretical predictions of structure.

Scheme 3

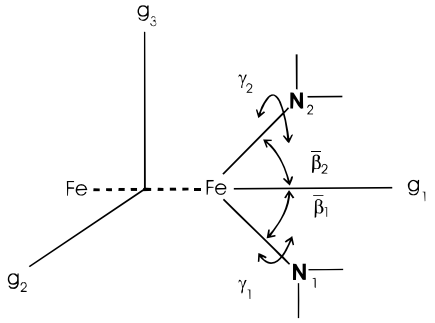

conserved [Cys/His] boxes must twist back upon itself to bring them parallel to each other" [see Figure 7 of Davidson *et al*. (1992) and Scheme 2).

We wondered if it would be possible to predict reasonable three-dimensional structures of the Rieske active site by applying the following constraints: (i) the relatively short sequence involved in providing the coordinating ligands to the [2Fe-2S] cluster, (ii) the looping of the sequence between the two Cys/His boxes, (iii) the requirement that both His residues be coordinated to one of the Fe atoms through their δ-N ring atoms, and (iv) the spatial arrangement of the two imidazole rings presented in Table 1 and illustrated in Scheme 3. In the case of the bc_1 and b_6f Rieske proteins, an additional constraint might be provided by the presence of a disulfide bond between additional conserved Cys residues (noted by in Figure 6, *c* and *d*) as previously suggested by Davidson *et al*. (1992) (Scheme 2).

Accordingly, we chose two segments of the amino acid sequence of *Rh. capsulatus* Rieske protein (Figure 6, c), peptide 1 (CysThrHisLeuGlyCys) and peptide 2 (CysProCysHis), for this study. We began with idealized coordinates taken from plant ferredoxins (Mouesce *et al*., 1994), replacing two of the cysteine ligands with imidazoles, with an Fe−N bond length of 2.1 Å and a α (*cf.* Table 1) of zero.[5] Since the γ angle is not determined from the current ENDOR data, and β is allowed to range between 35 and 50°, we conducted conformational searches to see which combinations of the β and γ angles were forbidden due to steric overlap in just the core region. Figure 7 shows these allowed ranges of angles, determined primarily by the requirement that the two histidine ligands not sterically overlap each other, and to a lesser extent by the requirement that the histidine rings avoid clashes with the inorganic sulfurs.

Of the 250 structures calculated, all had two features in common. First, the structures tended to wrap the peptide chains around the iron-sulfur cluster so that one of the inorganic sulfurs and the two iron atoms were completely buried, while the other inorganic sulfur atom was exposed. In addition, the buried sulfur was often hydrogen-bonded to one or more amino hydrogens of the peptide group. Using the criteria that a hydrogen bond is formed when the H−S distance is ≤2.6 Å and the N−H−S angle is ≥120°, 93 of the 250 structures have one or more hydrogen bonds to the buried sulfur. The most common donors are the His of peptide 1, with a hydrogen bond present in 33 of the structures, the noncoordinating Cys of peptide 2 (29 instances), and the His of peptide 2 (24 instances). Almost none of the structures have hydrogen bonds to the exposed sulfur atom. Following the previous suggestion of Davidson *et al.* (1992), a disulfide bond was incorporated between the noncoordinating Cys residues in the two peptides, and a second common feature of the resulting structures involved the placement of this disulfide bond. Since the two histidines are not equivalent, the plane defined by the N(δ) atoms of the imidazoles and the iron atoms has two distinct sides. Interestingly, the structures fall into two groups easily distinguished by the distance between the midpoint of the disulfide bond and the Fe,N(δ) plane. In about half of the structures, the minimum value of this distance is ≥3.8 Å *above* the plane (these structures are labeled *up*), while in the other half, the distance is ≥3.4 Å *below* the plane (these structures are labeled *down*). There was no significant difference in the average energies of these families of structures. The *down* arangement is indicated in Scheme 2. Representatives of the two families of structures are shown in Figure 8, where the presence of one "buried" and one "exposed" inorganic sulfur can also be seen. For visual clarity, a single example taken from Figure 8 is presented as a stereoview in Figure 9.

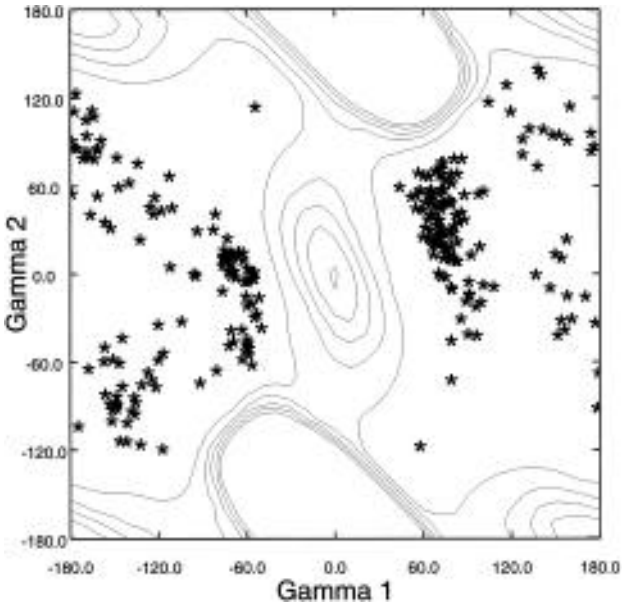

FIGURE 7: Analysis of the histidine γ_1 and γ_2 angles. Contours indicate regions of steric overlap for $\beta = 50°$; patterns for $\beta = 40°$ are similar. Steric overlaps were determined using the following atomic radii: H, 0.95 Å; N, 1.35 Å; O, 1.30 Å; C, 1.45 Å; S, 1.80 Å; and Fe, 1.80 Å. Asterisks show the final values of the γ angles in the refined structures. Almost all of the structures on the right side of the figure are *up* (see text), and almost all on the left are *down*.

Figure 8 also shows that the location of the disulfide bond relative to the iron−sulfur core determines the general nature of the peptide chain trace, but not its details. Analyses of peptide hydrogen bonds reveal structural features in addition to the overall *up/down* classification. The ThrHisLeuGly sequence in peptide 1 formed a β turn in 46 of the structures, with an $i \rightarrow i+3$ hydrogen bond between the carbonyl of the threonine residue and the amide hydrogen of the Gly; 36 of these structures were *down*. A similar tight β turn was formed from residues CysProCysHis of peptide 2 in 13 structures, of which 11 were *up*. Even where these hydrogen bonds are not formed, the peptide backbone tends to have a

[5] EXAFS studies of PDO by Tsang *et al*. (1989) indicate Fe−N bond lengths of 2.05 Å and terminal Fe−S bond lengths of 2.32 Å.

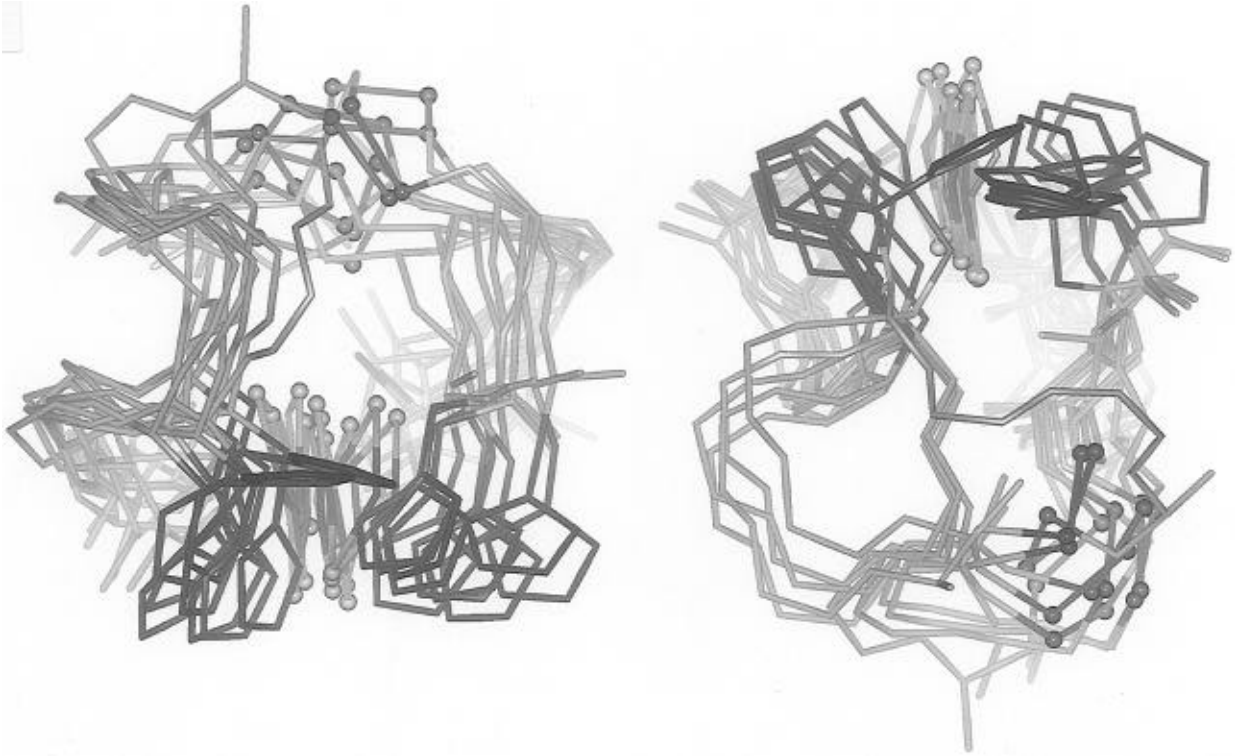

FIGURE 8: Representative structures of the *up* (left) and *down* (right) families of structures. The 10 lowest-energy structures in each family are shown, superimposed on the active site core and the peptide backbone. Peptide 1 is at the left and peptide 2 at the right. Cysteine (toward the back) and histidine (toward the front) side chain atoms are shown, and others are omitted. The inorganic sulfur atoms and the sulfur atoms in the disulfide bridge are indicated by spheres.

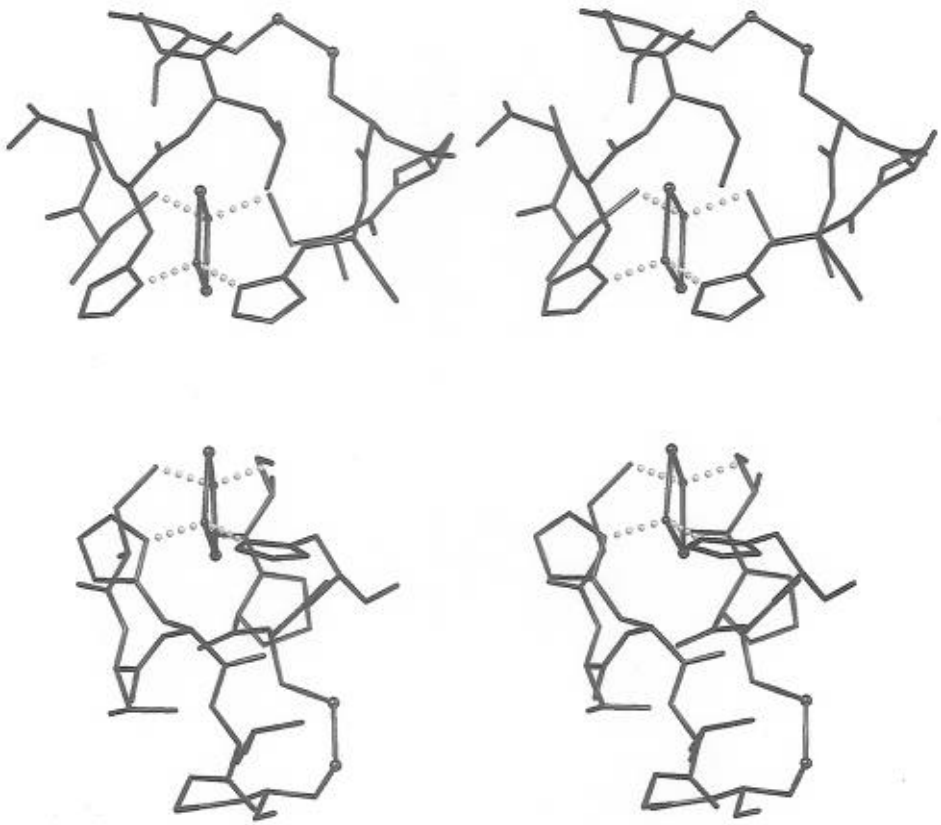

FIGURE 9: Stereo presentation of representative *up* (top) and *down* (bottom) model structures selected from Figure 8. The view is nominally along the Fe−Fe axis with one of the bridging S atoms "internal" to the structure. Peptide 1 is on the right, and the disulfide is shown by the two balls on the right side in both structures.

chain reversal at these points. A cross-strand hydrogen bond between the carbonyl of Pro in peptide 2 and the amide hydrogen of Thr in peptide 1 was found in 10 structures. Nine of these cross-strand structures were *down*. Since potential hydrogen bonds to other parts of the protein are not included in this model, it is not surprising that some of

the lowest-energy structures contained this interaction.

The γ angles of the final structures are shown in Figure 7. Although they were not restrained during the annealing stage, γ_1 showed two preferred ranges, with 76 structures in the interval [60°,90°] (*pos*) and 50 structures in the interval [−80°,−50°] (*neg*). No γ_1 angles were found in the interval [−40°,40°]. The γ_2 angle was more spread out, with 201 structures rather uniformly distributed over the interval [−90°,70°]. No γ_2 angles were found below −140° or above 130°. The γ_1 angles were strongly correlated with overall *up*−*down*, in that all 76 *pos* structures were *up* and 46 of 50 *neg* structures were *down*.

Overall, the segregation into *up* and *down* families corresponds to two possible "chiralities" for wrapping the polypeptide chain around the [2Fe-2S] cluster. Once this is determined, the general conformation of the chain and the location of the disulfide bond are roughly fixed, but within fairly loose bounds, as illustrated in Figure 8.

DISCUSSION

Nitrogen ENDOR and Molecular Modeling. Earlier studies of PDO(^{15}N(u)) (Gurbiel *et al.*, 1989) showed that two histidines are coordinated to the Fe^{2+} site of the [2Fe-2S] Rieske-type cluster. The present ENDOR examination of PDO(^{15}N(δ)) demonstrates that the two histidines are each ligated through N(δ), completing the structural model deduced from the previous ENDOR analysis. The results in Table 1 show that the ^{15}N hyperfine tensors for the Rieske centers of PDO and BC1 from *Rh. capsulatus* are effectively the same, supporting the additional conclusion that the proposed structure of the [2Fe-2S] cluster is similar in all Rieske-type proteins. The refined values of the hyperfine tensors reaffirm the essentials of the geometry proposed for the cluster (Gurbiel *et al.*, 1989, 1991). All the hyperfine tensors exhibit approximately axial behavior, where the unique axis A_3 corresponds to the Fe−N bond. Each center appears to have a slight but significant difference between the tensor components for N(1) and N(2), and the couplings for N(1) and N(2) of PDO are indistinguishable from those of their counterpart in BC1. However, it should be pointed out that the resolution of ^{15}N spectra from the bc_1 complex is much lower than that of PDO, a possible indication of greater structural flexibility in the Rieske center.

The ENDOR determination of the orientation of the ^{15}N-(δ) hyperfine tensors shows that the plane of the N−Fe−N bonds coincides with the g_1−g_3 plane of the **g** tensor and that the N−Fe−N angle between the two ligands is either $\beta_1 + \beta_2 \sim 80°$, bisected by g_3, or $\bar{\beta}_1 + \bar{\beta}_2 \sim 100°$ ($\bar{\beta}_i \equiv \pi/2 - \beta_i$), bisected by g_1. On structural grounds alone, the larger value seems more plausible. We tentatively assign g_1 along the Fe−Fe axis and g_2 along the S^{2-}−S^{2-} axis, resulting in an arrangement that is generally consistent with tetrahedral coordination geometry (see Scheme 3).

As is evident in Figure 8, the modeling studies indicate considerable flexibility in how the polypeptide backbone can wrap around the active site core, but certain patterns arise because of the *a priori* constraints. Thus, the putative disulfide linkage may lie either above or below (but not near) the plane of the iron and nitrogen atoms of the core. In addition, the models predict that one of the two inorganic sulfur atoms will be buried by intervening sequences [*cf.* Figure 6) while the other inorganic sulfur atom will be exposed to the remainder of the protein or to solvent. The predicted structures show generally tight turns or chain reversals at the ThrHisLeuGly and CysProCysHis positions, often stabilized by $i \rightarrow i+3$ hydrogen bonds. It is possible to form hydrogen bonds between amide protons of the histidine or cysteine ligands and the buried inorganic sulfur; the presence of these may influence redox or electron transport properties of the active site. It will be of interest to compare these models with eventual crystal structure determinations. Since the modeling approach described here could easily be extended to other sequences, it may also be of use in constructing models of homologous proteins.

Iron ENDOR. The ^{57}Fe ENDOR patterns recorded throughout the EPR envelope by a combination of CW and pulsed ENDOR techniques have allowed us to determine the full hyperfine tensors of the ferrous and ferric sites, including their principal values and orientations relative to the **g** tensor axes (Table 2). It should be pointed out that neither of the two techniques alone would be able to achieve these results. A Mössbauer study of the Rieske-type center in *T. thermophilus* (Fee *et al.*, 1984) reported hyperfine tensor components of Fe^{3+} and Fe^{2+} that are indistinguishable from those reported in Table 2 if one assigns the more strongly coupled Fe_A to the ferric site and the highly anisotropic Fe_B to the ferrous site. The ENDOR analysis further shows that these two tensors are coaxial with the **g** tensor and that the unique, large, hyperfine value of the axial $^{57}Fe_B^{2+}$ tensor lies along g_1.

The ^{57}Fe hyperfine tensors are qualitatively the same as those reported for the [2Fe-2S] centers of adrenodoxin and plant ferredoxin as summarized in Table 2. In particular, in all cases, the ferrous ion hyperfine tensor is axial, with the unique hyperfine tensor component being largest ($|A_{par}| \sim$ 33 MHz) and aligned along g_1. Therefore, these results do not support the hypothesis that the differences between [2Fe-2S] clusters in plant ferredoxins and Rieske-type complexes may be reflected by the orientation of the **g** tensor with respect to the Fe^{II}−Fe^{III} bond. There appears, however, to be quantitative differences between the tensors of the ferrous ions, with $A(Fe_B)$ for plant ferredoxins and PDO being more nearly axial and having larger values for $\Delta A = |A_{||} - A_{\perp}|$ [$A_{||} = A_1$ and $A_{\perp} = (A_2 + A_3)/2$] than that of "non-plant" [Fe_2S_2] centers (e.g. adrenodoxin). The ferredoxin Fe^{3+} hyperfine tensor is effectively axial, while the other two are distinctly rhombic; all three types of clusters have the unique or smallest hyperfine component of ∼43 MHz which lies along g_1.

By contrast, the quadrupole electric field gradient (**EFG**) tensor at the ferrous ion site of the Rieske-type centers, as determined by Mössbauer spectroscopy (Fee *et al.*, 1984), differs sharply from that of the plant ferredoxins (Table 2). The EFG in ferredoxin is axial, with a unique component that is negative and parallel to $A_{||}$; for the Rieske centers, the tensor again is axial, but the unique component is positive and lies perpendicular to $A_{||}$ (see Appendix). Bertrand and Gayda (1979) have developed a model which suggests that the properties of the cluster are governed by the rhombicity of the Fe^{2+} site. The **g** tensor of a ferric ion is essentially isotropic, and thus, according to eq 1, the anisotropy of the cluster **g** tensor is determined by the individual tensor of the $Fe^{2+}(d^6)$ ion. The environment of the Fe^{2+} ion is characterized as a tetragonally distorted tetrahedron. This "crystal field" splits and mixes *d* orbitals [*cf.* Bertrand *et al.*

(1985, 1991)], with the orbital that contains the the sixth d electron being written as

$$|\phi_o\rangle = \cos\theta|z^2\rangle + \sin\theta|x^2 - y^2\rangle \quad (3)$$

Within this model, the anisotropic **g** and **A** tensors and also the **EFG** tensor for Fe^{2+} are functions of the parameter θ, along with the *d* orbital energy spacings. We have rewritten the Bertrand−Gayda expressions, including modifications by Hearshen *et al.* (1986), and they are presented in the Appendix.

The Bertrand−Gayda model, as applied to Rieske-type centers, yields a *d* electron contribution to the **EFG** of Fe^{2+} that agrees with experiment both in sign and in orientation with respect to $\mathbf{A}_2$, when one takes $|\theta| \approx \pi/6$, corresponding to a "$d_{y^2-z^2}$" orbital. However, it predicts the wrong orientation of the ferrous ion hyperfine tensor relative to the cluster **g** tensor as well as unsatisfactory values for its principal components (Table 2). Our experiments indicate that the unique component of the axial hyperfine tensor of Fe_B is largest and lies along $g_1 = g_{max}$; the Bertrand-Gayda model predicts that the unique component is the smallest and places $|A_{min}|$ along g_1. One reason for these discrepancies may be contributions from coupled (cluster) spin states having $S > {}^1/_2$. This seems unlikely because they would be expected to also cause unusual anisotropies at the ferric site (Sage *et al.*, 1989), which are not observed. A direct determination of the electronic spin coupling would settle this issue. A second reason may be that Rieske centers are described by a "d_{z^2}" ground state ($\theta \approx 0$), as for the plant ferredoxins (Münck *et al.*, 1972). If so, the principal values of $\mathbf{A_2}$ and its orientation relative to **g** are predicted correctly. However, the corresponding prediction for the d electron contribution to the **EFG** does not agree with experiment, with respect to sign of the unique component, its relative magnitudes, or its orientation relative to $\mathbf{A}_2$ (Appendix). Thus, if this interpretation holds, the difference between the **EFG** tensors of the two classes of [2Fe-2S] proteins must reflect contributions to the **EFG** from the other d electrons on the high-spin Fe^{2+} ($S = 2$) (and ligand electrons) that are caused by the $(His)_2$ coordination of the Rieske-center Fe^{2+} ion. In plant ferredoxins, the Fe^{2+} (d^6 ion) is coordinated to four sulfur atoms (two S^{2-} and two cys S^-) in approximately tetrahedral geometry, with five of the d electrons having essentially spherical symmetry, thus not contributing to the **EFG**, while the sixth d electron on Fe^{2+} dominates its **EFG**. However, it seems reasonable to suggest that, in the Rieske-type centers, differential charge delocalization to the two S^{2-} and the two Nδ of the His ligands deforms the charge density of the half-filled d^5 subshell to the point that it makes a dominant contribution to the **EFG**. This suggestion is in keeping with the early remarks of Münck and co-workers who cautioned against oversimplified interpretations of **EFG** (and hyperfine) components (Fee *et al.*, 1984). In our opinion, these high-precision ENDOR results indicate large gaps in our understanding of the electronic structures of the simplest [2Fe-2S] clusters and the need for further examination.

This report shows that it is possible to apply knowledge of structural constraints derived from comparative sequence analyses and from ENDOR spectroscopy and to use molecular-modeling techniques to obtain detailed predictions of the geometrical structure of a metal cluster prosthetic group *and* of the coordinating polypeptide chain, thereby achieving a more complete picture of the active site. The ^{57}Fe data resolve experimental ambiguities about the spin-Hamiltonian parameters of the Rieske [2Fe-2S] cluster and in so doing disclose the incompleteness of our understanding of even the simplest Fe−S cluster.

ACKNOWLEDGMENT

We thank Drs. R. Olsen of The University of Michigan and G. Zylstra of Rutgers University for construction of the DB0110 mutant and Dr. Bill Bachovchin of Tufts University for supplying the ^{15}N-labeled histidine used in this and the previous work.

APPENDIX

Further insights into the electronic and geometric properties of the Rieske center require a joint analysis of the **g**, $\mathbf{A}_2$, and Fe quadrupole tensors. The mixed-valence, [2Fe-2S]$^{1+}$ center exhibits an $S = {}^1/_2$ ground state because of antiferromagnetic spin coupling between valence-localized Fe^{3+} ($S = {}^5/_2$) and Fe^{2+} ($S = 2$) ions. Equation A1 gives the relationship between the resulting cluster **g** tensor and the individual ion g tensors, as well as that between the observed hyperfine tensors for the two Fe sites and those of the individual ion tensors,

$$\mathbf{g} = \frac{7}{3}g_1 - \frac{4}{3}g_2 \quad \mathbf{A}_1 = \frac{7}{3}a_1 \quad \mathbf{A}_2 = -\frac{4}{3}a_2 \quad \text{(A1)}$$

where (g_1, a_1) refers to $Fe^{3+}{}_A$ and (g_2, a_2) to $Fe^{2+}{}_B$.

For our purposes, we rewrite the expressions of Bertrand and Gayda for g_2 and a_2 of an uncoupled ferrous ion, as corrected by Hearshen *et al.* (1986), as follows

$$g_{2j} = g_e + \Delta g_{2i}$$

$$a_{2x} = a_2 - \frac{P}{4}\left[\frac{4}{7}[1 - 2\sin^2(\theta+\pi/3)] + \Delta g_{2x}\right] \equiv a_2 - \frac{P}{4}\left[\frac{4}{7}\mathbf{X}(\theta) + \Delta g_{2x}\right]$$

$$a_{2y} = a_2 - \frac{P}{4}\left[\frac{4}{7}[1 - 2\sin^2(\theta-\pi/3)] + \Delta g_{2x}\right] \equiv a_2 - \frac{P}{4}\left[\frac{4}{7}\mathbf{Y}(\theta) + \Delta g_{2y}\right]$$

$$a_{2z} = a_2 - \frac{P}{4}\left[\frac{4}{7}(1 - 2\sin^2\theta) + \Delta g_{2z}\right] \equiv a_2 - \frac{P}{4}\left[\frac{4}{7}\mathbf{Z}(\theta) + \Delta g_{2z}\right] \quad \text{(A2)}$$

where θ is defined in eq 3 (see Discussion), $a_2 \approx -19.2$ MHz is the contact term, and $P \approx 55$ MHz. The *g*-shifts, Δg_{2i}, are functions of θ and *d* orbital energy spacings that need not be specified here. Instead, they are calculated from eq A1, using the experimental **g** tensor and the procedure of Bertrand and Gayda to treat the ferric ion **g** tensor. The θ-dependent contributions to the a_{2i}, $\mathbf{X}(\theta)$, $\mathbf{Y}(\theta)$, and $\mathbf{Z}(\theta)$, represent the electron-nuclear dipolar interaction with the sixth electron on Fe^{2+} (eq A2). If the other d electrons form a spherical subshell, then d electrons contributions to the principal values predicted for the **EFG** tensor at Fe^{2+}, **V**,

can be written

$$V_{2x} = -4\mathbf{V}\cdot\mathbf{X}(\theta)$$

$$V_{2y} = -4\mathbf{V}\cdot\mathbf{Y}(\theta) \qquad \text{(A3)}$$

$$V_{2z} = -4\mathbf{V}\cdot\mathbf{Z}(\theta)$$

so as to emphasize the connection between **V** and the dipolar contribution to the anisotropic part of **A** ($\mathbf{V} \propto |e|\langle R^{-3}\rangle$) (eq A3).

The Fe^{2+} ion of plant ferredoxins is characterized by an axial hyperfine tensor whose unique component (A_{2z}) is largest and lies along g_1. The Fe^{2+} ion has an axial quadrupole tensor ($\eta \approx 0$) whose unique component, $V_{2z'}$, is negative; it lies along A_{2z} and thus g_1. All this can be explained by an Fe^{2+} ($S = 2$) ion with a "d_{z^2}" ground state, namely $\theta \approx 0$ in eq 3 (see Discussion).

The Rieske centers have qualitatively similar **g** tensors ($g_{av} < 2$) but quantitatively different *g*-values. The Fe^{2+} site hyperfine tensor is like that for the plant ferredoxins, namely axial with the unique component having the largest magnitude. The Fe^{2+} site has an axial quadrupole tensor ($\eta \sim 0$), but the unique value $V_{2z'}$ is positive not negative and lies along the smallest component of the hyperfine tensor, not the largest.

Bertrand and Gayda interpret this by assigning $\theta \approx -\pi/6$ which corresponds to a "$d_{y^2-z^2}$" orbital for the sixth electron. This predicts that the unique **EFG** component ($V_{2z'}$) coincides with the smallest hyperfine component (A_{2y}). Our experiments show that this approach aligns the **g** and $\mathbf{V}_2$ tensors correctly. Although the calculation of the hyperfine components with eq A3 gives a hyperfine tensor that is close to axial for any assumed assignment of crystal field (*x*, *y*, or *z*) axes to the observed **g** tensor axes, it gives the unique component as having the *smallest* magnitude, not the largest. Upon considering the dependence of the *g*-values on θ, they assign $g_1 \leftrightarrow g_y$ because g_y should be least sensitive to fluctuations in θ at $\theta = -\pi/6$ and from this deduce orbital energies. They suggest this assignment can be tested by ENDOR, and in fact, our measurements show it to be in error, for $|A|_{max}$ lies along g_1, not $|A|_{min}$.

Hearshen *et al.* (1986) in essence adopt the Bertrand and Gayda model to explain the Fe^{2+} quadrupole tensor.[6] They choose to evaluate the model solely in terms of **A** tensor anisotropy and the **EFG** tensor and do not interpret **g** in detail. Their approach has the virtues of the Bertrand and Gayda model insofar as it correctly predicts the sign of $V_{2z'}$ and the orientation of $\mathbf{V}_2$ with respect to $\mathbf{A}_2$, but again it predicts that $\mathbf{A}_2$ is nearly axial with $|A_2|_{min}$ being the unique value, not $|A_2|_{max}$. By decoupling the discussion of **g**, Hearshen *et al.* (1986) are free to assign the relative orientations of $\mathbf{A_2}$ and g_1, and they take $g_z \leftrightarrow g_1$. To the extent that the calculation gives A_{2z} as the largest component in magnitude, if only by a slight amount, this correctly anticipates our experiments.

The unsatisfying prediction for the A_{2i} is *intrinsic* to the structure of the equations themselves, as can be seen by our rewriting of the Bertramd−Gayda expressions (eq A2). It is clear that the experimental *g*-values for the coupled system ($g_1 \sim 2$, $g_2 \sim 1.9$, $g_3 \sim 1.8$) must correspond to a set of values (Δg_1, Δg_2, and $\Delta g_3 \approx <\sim 0.5$, $<\sim 0.15$, and $<\sim 0.2$). Even if one takes into account the reservations expressed by Hearshen *et al.* (1986) about this procedure, in this case, the anisotropic contribution to the hyperfine couplings predicted by eq A2 is dominated by the electron nuclear dipolar interaction [$\mathbf{X}(\theta)$, $\mathbf{Y}(\theta)$, $\mathbf{Z}(\theta)$] and not the terms in Δg_{2i}; this conclusion is independent of the assignment of observed *g*-values (g_1, g_2, and g_3) to the Fe^{2+} ion crystal field directions (*x*, *y*, and *z*). In short, *within* this crystal field model, it appears to be inherently impossible to reconcile the observed $\mathbf{V}_2$ **EFG** tensor for Fe^{2+} PDO with the accompanying observation of an axial $\mathbf{A}_2$ hyperfine tensor ($|A_{2\|}| > |A_{2\perp}|$).

[6] The correspondence is somewhat obscured by the fact that they assign $\theta = +\pi/6$, not $-\pi/6$, which permutes axis labels and places V_z' and $|A|_{min}$ along *x* rather than *y*.

[7] The program nab is available via anonymous ftp as riscsm.scripps.edu/pub/nab5.ddmmmyy.tar.Z, where ddmmmyy is the file's creation date [see Macke (1996)].

REFERENCES

Abragam, A., & Bleaney, B. (1970) *Electron Paramagnetic Resonance of Transition Ions*, 2nd ed., Clarendon Press, Oxford.

Anderson, R. E., Dunham, W. R., Sands, R. H., Bearden, A. J., & Crespi, H. L. (1975) *Biochim. Biophys. Acta 408*, 306−322.

Bachovchin, W. W. (1986) *Biochemistry 25*, 7751−7759.

Batie, C. J., & Ballou, D. P. (1990) *Methods Enzymol. 188*, 61−70.

Batie, C. J., LaHaie, E., & Ballou, D. P. (1987) *J. Biol. Chem. 262*, 1510−1518.

Bertrand, P., & Gayda, J.-P. (1979) *Biochim. Biophys. Acta 579*, 107−121.

Bertrand, P., Guigliarelli, B., Gayda, J.-P., Beardwood, P., & Gibson, J. F. (1985) *Biochim. Biophys. Acta 831*, 261−266.

Bertrand, P., Guigliarelli, B., & More, C. (1991) *New J. Chem. 15*, 445−454.

Blaney, J. M., Crippen, G. M., Dearing, A., & Dixon, J. S. (1990) *DGEOM - Distance Geometry*, Quantum Chemistry Program Exchange, Bloomington, IN.

Blumberg, W. E., & Peisach, J. (1974) *Arch. Biochem. Biophys. 162*, 502−512.

Britt, R. D., Sauer, K., Klein, M. P., Knaff, D. B., Kriauciumas, A., Yu, C.-A., Yu, L., & Malkin, R. (1991) *Biochemistry 30*, 1892−1901.

Bull, C., & Ballou, D. P. (1981) *J. Biol. Chem. 256*, 12673−12680.

Crippen, G. M., & Havel, T. F. (1988) *Distance Geometry and Molecular Conformation*, Research Studies Press, Taunton, England.

Davidson, E., Ohnishi, T., Atta-Asafo-Adjei, E., & Daldal, F. (1992) *Biochemistry 31*, 3342−3351.

Davoust, C. E., Doan, P. E., & Hoffman, B. M. (1996) *J. Magn. Reson*. (in press).

Doan, P. E., Fan, C., Davoust, C. E., & Hoffman, B. M. (1991) *J. Magn. Reson. 95*, 196−200.

Fan, C., Doan, P. E., Davoust, C. E., & Hoffman, B. M. (1992) *J. Magn. Reson. 98*, 62−72.

Fee, J. A., Findling, K. L., Yoshida, T., Hille, R., Tarr, G. E., Hearshen, D. O., Dunham, W. R., Day, E. P., Kent, T. A., & Münck, E. (1984) *J. Biol. Chem. 259*, 124−133.

Fee, J. A., Kuila, D., Mather, M. W., & Yoshida, T. (1986) *Biochim. Biophys. Acta 853*, 153−185.

Fritz, J., Anderson, R., Fee, J., Palmer, G., Sands, R. H., Orme-Johnson, W. H., Beinert, H., Tsibris, J. C. M., & Gunsalus, I. C. (1971) *Biochim. Biophys. Acta 253*, 110−133.

Gemperle, C., & Schweiger, A. (1991) *Chem. Rev. 91*, 1481−1506.

Gippert, G. P., Yip, P. F., Wright, P. E., & Case, D. A. (1990) *Biochem. Pharmacol. 40*, 15−22.

Gurbiel, R. J., Batie, C. J., Sivaraja, M., True, A. E., Fee, J. A., Hoffman, B. M., & Ballou, D. P. (1989) *Biochemistry 28 (11)*, 4861−4871.

Gurbiel, R. J., Ohnishi, T., Robertson, D., Daldal, F., & Hoffman, B. M. (1991) *Biochemistry 30*, 11579−11584.

Gurbiel, R. J., Fann, Y.-C., Surerus, K. K., Werst, M. M., Musser, S. M., Doan, P. E., Chan, S. I., Fee, J. A., & Hoffman, B. M. (1993) *J. Am. Chem. Soc. 115*, 10888−10894.

Hearshen, D. O., Hagen, W. R., Sands, R. H., Grande, H., Crespi, H. L., Gunsalus, I. C., & Dunham, W. R. (1986) *J. Magn. Reson. 69*, 440−459.

Hoffman, B. M., DeRose, V. J., Doan, P. E., Gurbiel, R. J., Houseman, A. L. P., & Telser, J. (1993) in *Biological Magnetic Resonance* (Berliner, L., & Reuben, J., Eds.) Vol. 13, pp 151−218, Plenum Press, New York.

Hunkapiller, M. W., Smallcombe, S. H., Whitaker, D. R., & Richards, J. H. (1973) *Biochemistry 12*, 4732−4743.

Liebl, U., Pezennec, S., Riedel, A., Kellner, E., & Nitschke, W. (1992) *J. Biol. Chem. 267*, 14068−14072.

Liljas, A., Kannan, P. C., Bergsten, I., Waara, K., Fridborg, B., Standberg, U., Carlbom, L., Jarup, S., Lovgren, & Petef, M. (1972) *Nat. New Biol. 235*, 131−137.

Macke, T. J. (1996) Ph.D. Thesis, The Scripps Research Institute, La Jolla, CA.

Mason, J. R., & Cammack, R. (1992) *Annu. Rev. Microbiol. 46*, 277−305.

Moore, J. M., Lepre, C., Gippert, G. P., Chazin, W. J., Case, D. A., & Wright, P. E. (1991) *J. Mol. Biol. 221*, 533−555.

Mouesce. J.-M., Chen, J. L., Noodleman, L., Bashford, D., & Case, D. A. (1994) *J. Am. Chem. Soc. 116*, 11898−11914.

Münck, E., Debrunner, P. G., Tsibris, J. C. M., & Gunsalus, I. C. (1972) *Biochemistry 11*, 85−93.

Neidle, E., Shapiro, M. K., & Ornston, N. (1987) *J. Bacteriol. 169*, 5496−5503.

Peishoff, C. E., & Dixon, J. S. (1992) *J. Comput. Chem. 13*, 565−569.

Rieske, J. S. (1976) *Biochim. Biophys. Acta 456*, 195−243.

Sage, J. T., Xia, Y.-M., Debrunner, P. G., Keough, D. T., de Jersey, J., & Zerner, B. (1989) *J. Am. Chem. Soc. 111*, 7239−7247.

Sands, R. H., & Dunham, W. R. (1975) *Q. Rev. Biophys. 7*, 443−504.

Shergill, J. K., & Cammack, R. (1994) *Biochim. Biophys. Acta 1185*, 35−42.

Trumpower, B. L. (1990) *Microbiol. Rev. 54*, 101−129.

Trumpower, B. L., & Gennis, R. B. (1994) *Annu. Rev. Biochem. 63*, 675−716.

Tsang, H., Batie, C. J., Ballou, D. P., & Penner-Hahn, J. E. (1989) *Biochemistry 28*, 7233−7240.

Weiner, S. J., Kollman, P. A., Nguyen, D. T., & Case, D. A. (1986) *J. Comput. Chem. 7*, 230−252.

Werst, M. M., Davoust, C. E., & Hoffman, B. M. (1991) *J. Am. Chem. Soc. 113 (5)*, 1533−1538.

BI960380U